

# Role of Oxygen Vacancy Ordering and Channel Formation in Tuning Intercalation Pseudocapacitance in Mo Single-Ion-Implanted $\text{CeO}_{2-x}$ Nanoflakes

Xiaoran Zheng,\* Sajjad S. Mofarah,\* Alan Cen, Claudio Cazorla, Enamul Haque, Ewing Y. Chen, Armand J. Atanacio, Madhura Manohar, Corey Vutukuri, Joel Luke Abraham, Pramod Koshy,\* and Charles C. Sorrell

Cite This: *ACS Appl. Mater. Interfaces* 2021, 13, 59820–59833

Read Online

ACCESS |

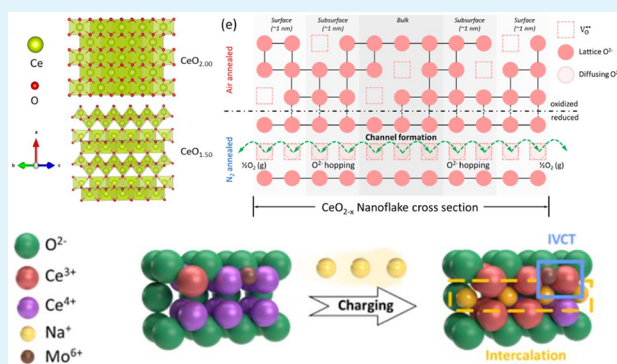
Metrics & More

Article Recommendations

Supporting Information

**ABSTRACT:** Metal oxide pseudocapacitors are limited by low electrical and ionic conductivities. The present work integrates defect engineering and architectural design to exhibit, for the first time, intercalation pseudocapacitance in  $\text{CeO}_{2-x}$ . An engineered chronoamperometric electrochemical deposition is used to synthesize 2D  $\text{CeO}_{2-x}$  nanoflakes as thin as  $\sim 12$  nm. Through simultaneous regulation of intrinsic and extrinsic defect concentrations, charge transfer and charge–discharge kinetics with redox and intercalation capacitances together are optimized, where reduction increases the gravimetric capacitance by 77% to  $583 \text{ F g}^{-1}$ , exceeding the theoretical capacitance ( $562 \text{ F g}^{-1}$ ). Mo ion implantation and reduction processes increase the specific capacitance by 133%, while the capacitance retention increases from 89 to 95%. The role of ion-implanted  $\text{Mo}^{6+}$  is critical through its interstitial solid solubility, which is not to alter the energy band diagram but to facilitate the generation of electrons and to establish the midgap states for color centers, which facilitate electron transfer across the band gap, thus enhancing n-type semiconductivity. Critically, density functional theory simulations reveal, for the first time, that the reduction causes the formation of ordered oxygen vacancies that provide an atomic channel for ion intercalation. These channels enable intercalation pseudocapacitance but also increase electrical and ionic conductivities. In addition, the associated increased active site density enhances the redox such that the 10% of the  $\text{Ce}^{3+}$  available for redox (surface only) increases to 35% by oxygen vacancy channels. These findings are critical for any oxide system used for energy storage systems, as they offer both architectural design and structural engineering of materials to maximize the capacitance performance by achieving accumulative surface redox and intercalation-based redox reactions during the charge/discharge process.

**KEYWORDS:** ceria 2D nanoflakes, ion implantation, defect engineering and architectural design, oxygen vacancy ordering and channel formation, surface and intercalation pseudocapacitance



## 1. INTRODUCTION

Metal oxide pseudocapacitors have become leading candidates for novel renewable energy storage devices owing to their greater power and energy densities compared to electrical double-layer capacitors,<sup>1</sup> longer cycling lives compared to metal–organic framework pseudocapacitors,<sup>2</sup> and oxidation resistance compared to metal dichalcogenide pseudocapacitors.<sup>3</sup> However, the performance of transition metal oxide pseudocapacitors such as  $\text{RuO}_2$ ,  $\text{MnO}_2$ , and  $\text{Fe}_2\text{O}_3$  is limited by surface-level reactions.<sup>4–8</sup> The main strategy used to enhance performance is architecture engineering to synthesis 2D morphology with high surface areas or heterojunction engineering for hybrid capacitors, typically with graphene or MXene.<sup>9,10</sup>

A state-of-the-art strategy is to generate a significantly higher area for electrolyte ion adsorption through atomic structural engineering for improving ionic permeation, thus enabling intercalation pseudocapacitance. The mechanism of intercalation pseudocapacitance is contributed from the intrinsic crystal structure offering two-dimensional (2D) fast ion diffusion channels for ion intercalation/deintercalation by charging and discharging. However, the intercalation pseudocapacitor is

Received: July 30, 2021

Accepted: November 24, 2021

Published: December 7, 2021



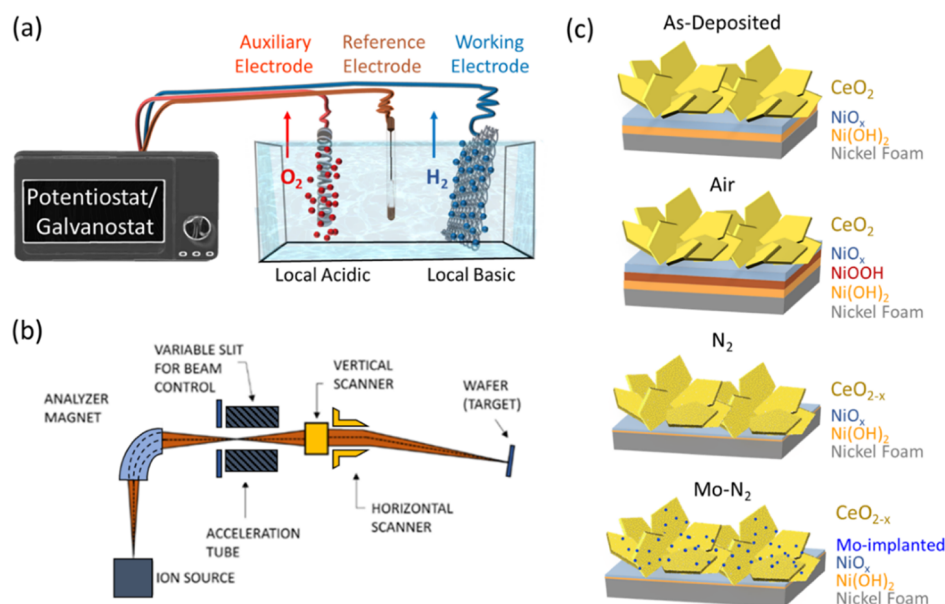


**Figure 1.** Schematic of the synthesis process of  $\text{CeO}_{2-x}$  nanoflakes on Ni foam substrates: (a) electrodeposition of  $\text{CeO}_{2-x}$  on the substrate; (b) schematic of the low-energy ion implantation method; (c) schematic of different types of  $\text{CeO}_{2-x}$  on the Ni foam substrate (as-Deposited: after drying at room temperature, air: after annealing in air at 300 °C,  $\text{N}_2$ : after annealing in nitrogen at 300 °C; Mo- $\text{N}_2$ : after Mo ion implantation and annealing in nitrogen at 300 °C).

confined by the nature of the material and only few electrode materials show intercalation behavior, including  $\text{V}_2\text{O}_5$ ,  $\text{MoO}_3$ ,  $\text{WO}_3$ ,  $\text{Nb}_2\text{O}_5$ , and  $\text{TiO}_2$  (B).<sup>11–16</sup> While the structures of these transition metal oxides share the characteristic of possessing intrinsic structural channels, they were limited by intrinsic low electric conductivity.<sup>2</sup> Since cubic  $\text{CeO}_2$  does not possess intrinsic structural channels, although it can be engineered in the 2D form,<sup>17</sup> the prognosis for its application is as a surface redox pseudocapacitor. While some studies mention the intercalation behavior in  $\text{CeO}_2$ , they do not provide any evidence;<sup>18–20</sup> thus, there do not appear to be any reports showing that  $\text{CeO}_2$  has intercalation pseudocapacitance. The dense packing crystal structure-endowed intercalation ability has not been explored.

Concerning defect engineering, the most common approach is through acceptor doping, largely for the purpose of increasing the oxygen vacancy concentration ( $[\text{V}_\text{O}^{\bullet\bullet}]$ ), where  $\text{V}_\text{O}^{\bullet\bullet}$  acts as active sites for surface adsorption.<sup>13,21–27</sup> A less-common approach is through donor doping, which creates active sites in the form of metal vacancies of variable valence. The major impact of these defects on the electrochemical process of some metal oxide nanostructures recently has been reported,<sup>28–30</sup> while the formation of substitutional and interstitial solid solutions upon doping generally is associated with charge compensation by ionic (by vacancy formation), electronic (electron/hole formation), or redox ( $\text{Ce}^{3+}/\text{Ce}^{4+}$  switching) processes. Furthermore, such redox processes can be imposed during electrochemical processing stages.<sup>23</sup> Consequently, there is a critical but essentially unexplored role for dopant and matrix ions in charge/discharge energy storage devices through the potential leveraging of both redox and ionic charge compensation mechanisms.

These charge compensation mechanisms can be moderated by the often-overlooked charge-transfer processes, intervalence charge transfer (IVCT) and multivalence charge transfer (MVCT).<sup>31</sup> In the former process, electrons exchange between two ions, typically between co-dopants or between the dopant

ion and matrix ion. In the latter process, electrons can exchange between multiple dopant ions and matrix ions. These mechanisms can be employed in pseudocapacitance design and performance through the selection of acceptor versus donor doping nature, valence of the dopant ion, ready valence change through redox switching, and a controlled processing temperature and atmosphere to impose specific structural characteristics.

Concerning architectural design, the dimensionality of nanostructures represents one of the principal regulators of the energy and power densities of electrodes. 2D nanomaterials offer advantageous electronic properties that facilitate enhanced kinetics, deriving from high surface-to-volume ratios, therefore enhancing active site concentrations and short diffusion distances for charge transfer, thereby enhancing ionic charge transfer.<sup>32</sup> However, it is evident that the active sites are more likely to be located on the low-area nanosheet edge terminations rather than on the more stable high-area planar surfaces.<sup>33</sup> Consequently, the application of specific surface engineering strategies to impose active sites on these planes offers the potential for significant improvement in the functionality of such materials.

The present work combined defect engineering and architectural design. The architectural design leverages the capacity to synthesize pure  $\text{CeO}_{2-x}$  nanoflakes using a template-free electrodeposition technique. The planar defect engineering leverages formation of oxygen vacancy channels to enhance intercalation capacitance behavior, and heteroatom-implanted defect engineering is for redox charge compensation by the donor from Mo ion implantation to facilitate electroconductivity.

## 2. RESULTS AND DISCUSSION

The considerable flexibility of the process and the capacity to optimize the nanoflake morphology were demonstrated through the various permutations of the experimental parameters, including different precursors, temperatures, and

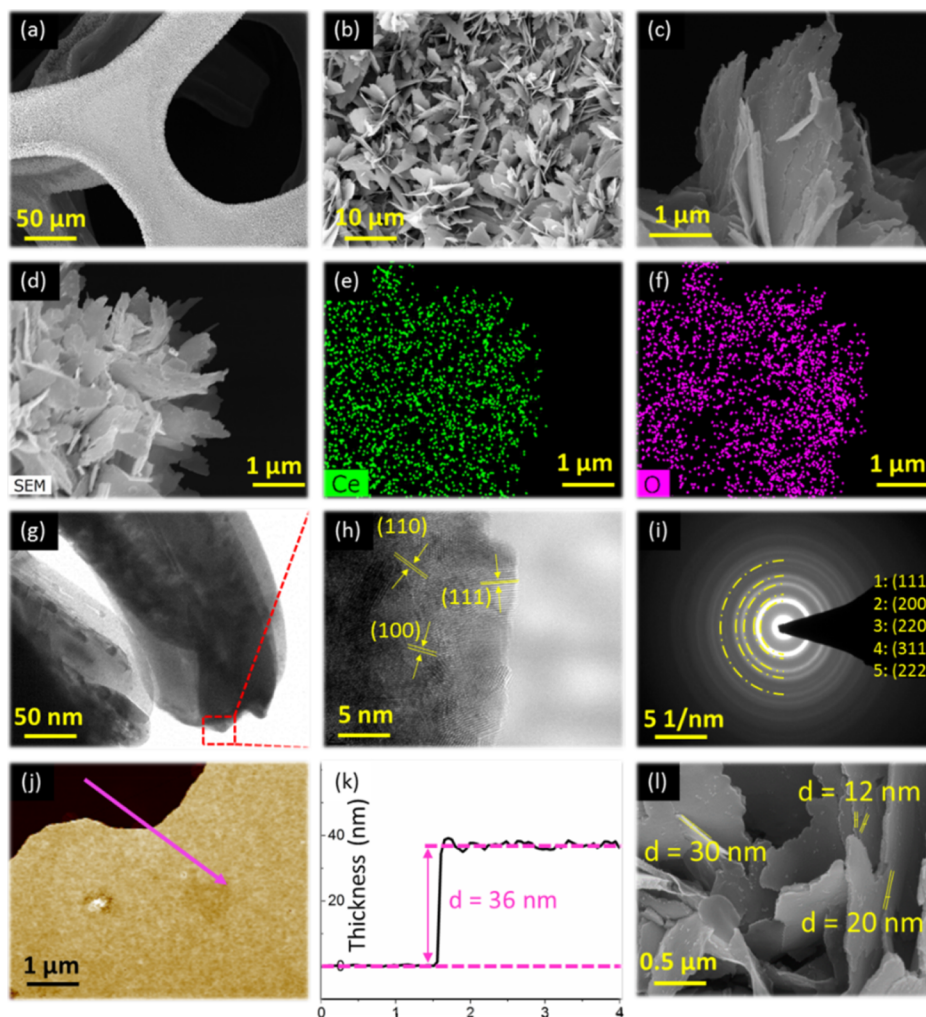


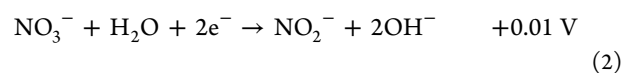
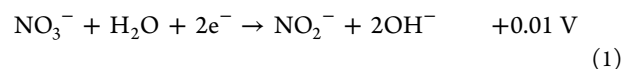
**Figure 2.** 2D  $\text{CeO}_{2-x}$  nanostructural features of  $\text{CeO}_{2-x}$  nanoflakes deposited on Ni foam substrates: (a) low-, (b) intermediate-, and (c) high-magnification SEM images; (d–f) SEM image and corresponding EDS mapping of (e) Ce and (f) O; (g,h) HRTEM images; (i) SAED pattern; (j) AFM image; (k) corresponding height profile; and (l) SEM image and thickness measurements.

substrates. The results of these studies are shown in Figures S2 and S3. The schematic of Figure 1 illustrates that the application of such suitable experimental parameters can result in the synthesis of free-standing  $\text{CeO}_{2-x}$  nanoflakes grown approximately vertically on the substrate. As stated, following this stage, donor defects were imposed in the  $\text{CeO}_{2-x}$  nanoflakes using Mo ion implantation. The defect equilibria subsequently were altered by atmospheric oxidation and reduction in air and  $\text{N}_2$ , respectively. This process also may have possibility to facilitate the imposition of acceptor Ni doping through diffusion from the Ni foam substrate into the nanoflakes.

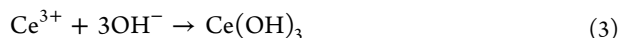
The scanning electron microscopy (SEM) image shown in Figure S4 reveals the formation of a surface layer that exhibited drying cracks. The Ni– $\text{H}_2\text{O}$  Pourbaix diagram, shown in Figure S5,<sup>34</sup> indicates that this as-electrodeposited surface layer derives from what probably was sequentially layered Ni foam/ $\text{Ni}(\text{OH})_2/\text{NiOOH}/\text{NiO}_x$ , as suggested by the thermodynamic study of this system by Barnard and Randell.<sup>35</sup> More critically, the Pourbaix diagram shows that the application of a negative voltage would shift the equilibria into the Ni metal predominance region, thereby partially or completely removing the passivating layer. The combined XPS, Raman, Pourbaix, and thermodynamic stability diagram data indicate the

formation of a hydroxide/oxide layer on the surface of the Ni foam during the soaking in the electrolyte (containing the oxidizing agent NaOH) for 10 min prior to electrodeposition. The formation of this layer was confirmed by additional Fourier transform infrared transmission (FTIR) spectroscopy data (Figure S6)<sup>36–38</sup> and energy dispersive spectroscopy (EDS) data (Figure S7) following progressive soaking in the electrolyte for 0, 10, and 20 min. Consequently, the  $\text{CeO}_{2-x}$  nanoflakes can form directly on the Ni metal surface, and subsequent annealing in air or  $\text{N}_2$  probably would alter this interface.

During electrodeposition using  $-1$  V versus Ag/AgCl, the pH would be expected to increase from the initial value of 6 at the reduction of dissolved  $\text{NO}_3^-$  (from  $\text{Ce}(\text{NO}_3)_3 \cdot 6\text{H}_2\text{O}$  and  $\text{NH}_4\text{NO}_3$ ) and at the decomposition of water<sup>39</sup>

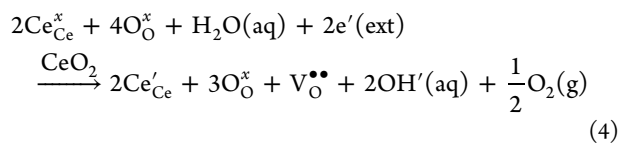


The resultant basic pH is required for the successful preliminary formation of  $\text{Ce}(\text{OH})_3$  on the Ni foam



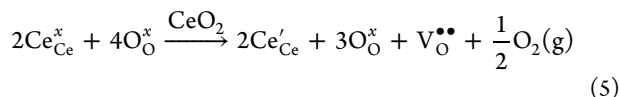
The Pourbaix diagram for the system Ce–H<sub>2</sub>O,<sup>31</sup> shown in Figure S8, reveals that the application of a negative voltage would increase the deposition of Ce(OH)<sub>3</sub> rather than forming CeO<sub>2-x</sub>. Thus, the Ce(OH)<sub>3</sub> → CeO<sub>2</sub> conversion takes place during annealing. As there is excess oxygen in Ce(OH)<sub>3</sub> for this conversion, it can take place in both air and N<sub>2</sub>.

Since electrodeposition involves the application of a voltage, it is possible to adapt the relevant Kröger–Vink defect equilibria for this process.<sup>40</sup> Since the standard reduction potential generated by the Ce<sup>4+</sup> + e' → Ce<sup>3+</sup> equilibria is +1.72 V,<sup>41</sup> the application of a negative voltage provides the driving force for Ce reduction and ionic charge compensation by V<sub>O</sub><sup>••</sup> formation in aqueous solution according to

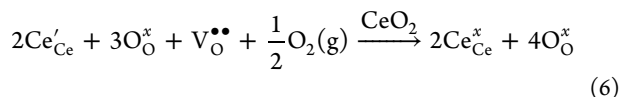


For pure CeO<sub>2-x</sub> subjected to different atmospheres, the intrinsic redox defect equilibria are as follows:<sup>31</sup>

Reduction



Oxidation



These intrinsic defect equilibria would be influenced by the potential extrinsic defect equilibria established through Mo<sup>4/5/6+</sup> ion implantation or Ni<sup>2+</sup> diffusion (less probability) from the Ni foam into the CeO<sub>2-x</sub> nanoflakes [Table S1 (using Mo<sup>5+</sup> as a model)]. While there appears to be no phase diagram for the system Mo–Ce–O, there is one for the system MoO<sub>3</sub>–CeO<sub>2</sub>.<sup>42</sup> The intermediate phases MoO<sub>3</sub>·3Ce<sub>2</sub>O<sub>3</sub> and MoO<sub>3</sub>·4Ce<sub>2</sub>O<sub>3</sub> suggest that these equilibria spontaneously shift Ce<sup>4+</sup> to Ce<sup>3+</sup>. Although this phase diagram does not indicate any solid solubilities, these effects often are not investigated as part of the experimental studies. However, the nature of ion implantation is such that stable or metastable solid solubility of Mo in CeO<sub>2</sub> is implicit. The favored Mo valence that can result during the processes of ion implantation and annealing under N<sub>2</sub> is shown in the Mo thermodynamic stability diagram (temperature pressure) of Figure S9, which indicates that Mo<sup>6+</sup> is the most stable valence. There is also no phase diagram for the system Ni–Ce–O, and there are no binary diagrams including NiO because it melts incongruently at 1422 °C.<sup>43</sup> The thermodynamic stability diagram for Ni (H<sub>2</sub>O–O<sub>2</sub> pressures), shown in Figure S10, confirms that Ni<sup>2+</sup> is the stable valence but also that the passivating layer would consist of Ni(OH)<sub>2</sub> + NiO.

SEM images of the CeO<sub>2-x</sub> nanoflakes are shown in Figure 2a–c. The low-magnification SEM image showing the Ni foam (Figure 2a) reveals homogeneous deposition of CeO<sub>2-x</sub> nanoflakes covering the surface. The intermediate-resolution SEM image (Figure 2b) shows that the nanoflakes grow independently, thus avoiding coarsening by intergrowth. The high-resolution SEM image (Figure 2c) reveals that the nanoflakes are laminated and curved and of several microns

width, with serrated edges. Elemental mapping of nanoflakes by EDS (Figure 2d–f) shows the base composition of the nanoflakes (Ce and O). Critically, Mo could not be detected, which is a result of the relative ion implantation dosage (1 × 10<sup>15</sup> atoms cm<sup>-2</sup>), which previously has been shown to not yield concentrations sufficiently high for detection,<sup>44,45</sup> especially for thin cross-sections.<sup>46</sup> However, the Mo dopant concentration is calculated to be ~1.7 mol % (Supporting Information).

The high-resolution transmission electron microscopy (HRTEM) image (Figure 2g) shows the smooth curvature of the nanoflakes; the enlargement (Figure 2h) reveals the nanoflakes' polycrystalline nature, as do the thickened diffraction rings of the selected area electron diffraction (SAED) pattern (Figure 2i). Atomic force microscopy (AFM) data (Figure 2j,k) indicate that the thickness of a randomly selected nanoflake was 36 nm.

Complementary SEM images of three nanoflakes reveal thicknesses in the range of 12–30 nm. These data highlight the advantageous architectural features of the nanoflakes for energy storage applications, which are high surface-to-volume ratios and short cross-sectional pathways for charge transfer. Furthermore, the defect equilibrium considerations support the view that these nanostructures may be equipped with high densities of accessible active sites in the forms of the intrinsic and extrinsic defects Ce<sup>3+</sup>, Mo<sup>4/5/6+</sup>, and V<sub>O</sub><sup>••</sup>.

The role of defects in energy storage applications was investigated for the as-electrodeposited CeO<sub>2-x</sub> nanoflakes subjected to annealing under air or N<sub>2</sub> (air and N<sub>2</sub>, respectively) and as-electrodeposited CeO<sub>2-x</sub> subjected to Mo ion implantation and annealing under N<sub>2</sub> (Mo–N<sub>2</sub>). The nanomorphologies were not altered during any of these processes.

The X-ray diffraction (XRD) patterns in Figure S11 show that the high roughness of the Ni foam prevents use of these data for lattice parameter determination. However, essentially identical samples were deposited on flat FTO substrates and ion-implanted, from which the lattice parameters were determined by Rietveld refinement, as given in Figure S12 and Table S2. These data show that as expected, the introduction of oxygen vacancies causes lattice contraction. Also, Mo ion implantation causes further lattice contraction, which is expected since, as will be discussed, the solid solubility mechanism is interstitial. Since then, in the CeO<sub>2</sub> crystal structure, the central interstice is surrounded by eight oxygen ions, which itself is surrounded by face-centered cubic cerium ions;<sup>31</sup> the occupation of the central interstice with a cation will cause lattice contraction.

The laser Raman microscopy (Raman) data, given in Table S2, are completely consistent with the XRD data in that they confirm progressively greater surface tension upon the introduction of oxygen vacancies and Mo ion implantation, both of which cause surface contraction relative to the bulk and consequent resultant surface tension. The X-ray photoelectron spectroscopy (XPS) data, which are discussed subsequently, confirm the detection of surface Mo in the Mo–N<sub>2</sub> sample.

Despite the inability of EDS to detect Mo, the combined XRD, Raman, and XPS data are mutually confirmatory in demonstrating that Mo is dissolved in the CeO<sub>2</sub> lattice. Parenthetically, it can be added that these data are consistent with both substitutional and interstitial solid solubility since Mo<sup>6+</sup> is smaller than Ce<sup>4+</sup>.<sup>47</sup>

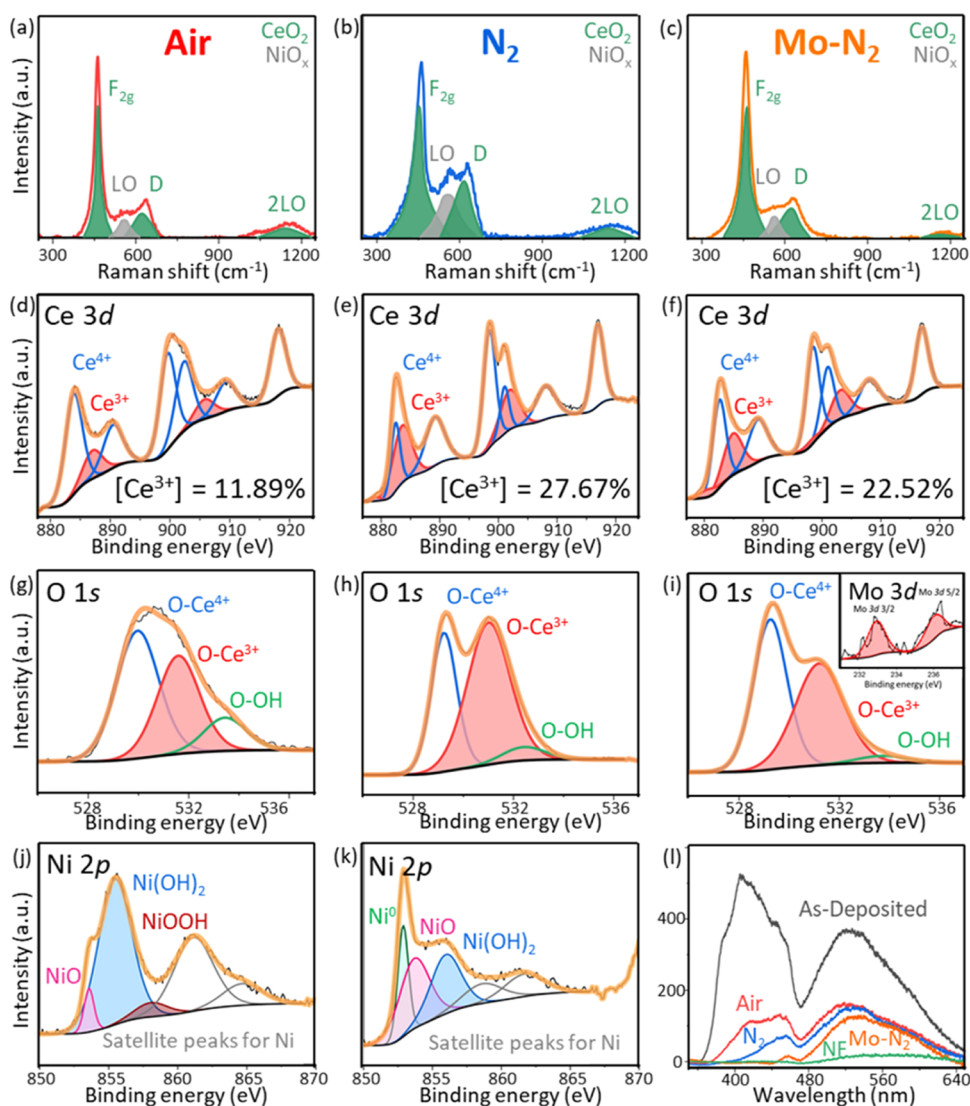


**Figure 3.** Defect analyses of  $\text{CeO}_{2-x}$  nanoflakes using different techniques: (a–c) laser Raman microspectra (identically scaled intensities): (a) air, (b)  $\text{N}_2$ , and (c)  $\text{Mo-N}_2$ ; XPS analysis of Ce 3d: (d) air, (e)  $\text{N}_2$ , and (f)  $\text{Mo-N}_2$ ; XPS analysis of O 1s: (g) air, (h)  $\text{N}_2$ , and (i)  $\text{Mo-N}_2$  (the inset image represents XPS analysis of Mo 3d); XPS analysis of Ni 2p: (j) air and (k)  $\text{N}_2$ ; and (l) PL spectra.

The Raman data (Figure 3a,b) show that sample  $\text{N}_2$  enhanced defect-associated intensities of the D and 2LO peaks of  $\text{CeO}_{2-x}$  compared to those of sample air, which is consistent with  $\text{V}_\text{O}^\bullet$  formation.<sup>48,49</sup> However, sample  $\text{Mo-N}_2$  (Figure 3c) showed decreased relative intensities, suggesting that Mo has a partially reversing effect. Supplementary Raman patterns of the Ni foam and  $\text{CeO}_{2-x}$  samples are shown in Figure S13.

The surface XPS data in the Ce 3d orbital are used for distinguishing  $\text{Ce}^{3+}$  (at the binding energy of  $\sim 881$  and  $\sim 885$  eV) and  $\text{Ce}^{4+}$  (at the binding energy of  $\sim 883$ ,  $\sim 889$ , and  $\sim 898$  eV).<sup>49–51</sup> The relatively subsurface defect is analyzed by O 1s XPS measurements of O– $\text{Ce}^{3+}$  (at a binding energy of  $\sim 531$  eV) and O– $\text{Ce}^{4+}$  (at a binding energy of  $\sim 529$  eV)<sup>52–55</sup> because of the higher penetration depth in O compared to that in Ce.<sup>56,57</sup> For  $\text{CeO}_{2-x}$ , Figure 3d–i shows that the  $\text{Ce}^{3+}$  concentrations ( $[\text{Ce}^{3+}]$ ) were relatively high for  $\text{CeO}_{2-x}$  and that sample  $\text{N}_2$  exhibited the highest value, again consistent with  $\text{V}_\text{O}^\bullet$  formation from atmospheric reduction under  $\text{N}_2$ . The partially reversing effect of Mo also is confirmed.

XPS data showed that  $\text{Mo}^{4+}$  is not present but that the valences  $\text{Mo}^{5+}$  and/or  $\text{Mo}^{6+}$  are present, as these peaks cannot be distinguished. However, the thermodynamic stability diagram (Figure S9) reveals that  $\text{Mo}^{6+}$  is stable under all of the experimental conditions used. Although, as stated, the XRD, Raman, and XPS data are mutually supportive of the solubility of Mo in  $\text{CeO}_2$ , the more sensitive technique proton-induced X-ray emission spectroscopy (PIXE) was used for further confirmation. As shown in Figure S14, pure Si was Mo ion-implanted in order to confirm the positions and relative intensities of the Mo peaks, and then, the spectra were obtained for  $\text{Mo-N}_2$ , thus confirming the solubility of Mo.

The XPS data for Ni (Figure 3j,k) confirm the presence of the components of the layered Ni-based structure. The photoluminescence (PL) data (Figure 3l) show that the recombination times are in the order Ni foam <  $\text{Mo-N}_2$  <  $\text{N}_2$  < air < as-deposited. However, since there is little difference between  $\text{Mo-N}_2$ ,  $\text{N}_2$  and air, this indicates that the charge carrier diffusion path is through the cross-sections of the nanoflakes, which are of unchanging thickness. The XPS data for Ce and Mo are deconvoluted in order to elucidate the

Table 1. Analysis of XPS Data for Pure and Mo-Implanted CeO<sub>2-x</sub> on Ni Foam

row	annealing atmosphere→	air		N <sub>2</sub>	
	parameter (atom %) ↓	CeO <sub>2-x</sub>	CeO <sub>2-x</sub>	Mo-CeO <sub>2-x</sub>	Mo-CeO <sub>2-x</sub> /CeO <sub>2-x</sub>
1	O/Ce ratio	3.53	5.27	4.48	0.85
2	Ce concentration	22.37	22.29	22.01	
3	surface <sup>a</sup> Ce <sup>3+</sup> /(Ce <sup>3+</sup> + Ce <sup>4+</sup> ) concentration	11.89	27.67	22.52	0.81
4	subsurface <sup>b</sup> O-Ce <sup>3+</sup> /(O-Ce <sup>3+</sup> + O-Ce <sup>4+</sup> ) concentration	43.47	63.15	49.54	0.78
5	subsurface <sup>b</sup> O-Ce <sup>3+</sup> /surface <sup>a</sup> Ce <sup>3+</sup>	3.66	2.28	2.19	
6	hypothetical surface <sup>a</sup> V <sub>O</sub> <sup>••</sup> concentration (atom %)	5.95	13.84	11.26	
7	hypothetical subsurface <sup>b</sup> V <sub>O</sub> <sup>••</sup> concentration (atom %)	21.74	31.57	24.77	
8	Mo/Ce ratio			0.01	

<sup>a</sup>Surface data based on Ce 3d XPS measurements as these data reflect Ce-O/Ce-OH surface bonds. <sup>b</sup>Subsurface data based on O 1s XPS measurements as these data reflect O-Ce subsurface lattice bonds.

effects of V<sub>O</sub><sup>••</sup> formation from atmospheric reduction and doping from ion implantation in Table 1. Although the XPS data for Ni were obtained, they were not considered, since they are indicative of the Ni foam rather than Ni dissolved in CeO<sub>2-x</sub>.

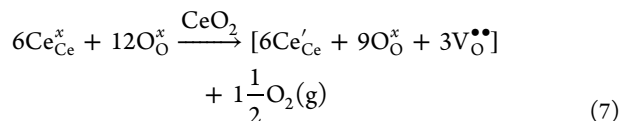
The data in Table 1 indicate the following:

Row 1: The O/Ce ratios are >2, which suggest high concentrations of cerium vacancies ([V<sub>Ce</sub><sup>'''</sup>]). However, values as high as 3.15 have been observed by others.<sup>56</sup> Although the intrinsic defect equilibria would involve the creation of two V<sub>O</sub><sup>••</sup> from reduction and charge compensation from the creation of one V<sub>Ce</sub><sup>'''</sup>, this actually would decrease the O/Ce ratio. Consequently, it is more likely that these data derive from the fact that the beam for oxygen detection has a greater penetration depth than that for cerium.<sup>23</sup>

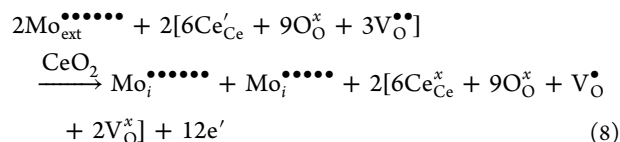
Row 2: These data confirm that V<sub>Ce</sub><sup>'''</sup> does not form upon reduction under N<sub>2</sub> or upon ion implantation and consequent Mo substitutional or interstitial solid solubility.

Row 3: The surface [Ce<sup>3+</sup>] values are more than double for CeO<sub>2-x</sub> annealed under N<sub>2</sub> compared to when annealed in air, resulting from Ce<sup>4+</sup> → Ce<sup>3+</sup> atmospheric reduction. Mo ion implantation and solid solubility partially reverse this situation. In terms of these two respective cases of intrinsic and extrinsic defect formations, the defect equilibria (i.e., combined redox and ionic charge compensation) would be as follows:

Intrinsic



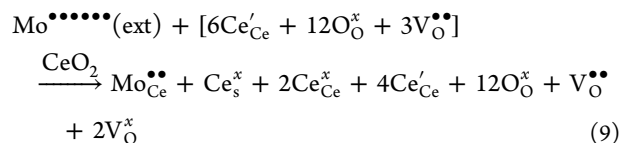
Extrinsic



Hence, the intrinsic defect equilibria during reduction increase the [Ce<sup>3+</sup>], but the extrinsic defect equilibria for combined Mo ion implantation and reduction result in Ce oxidation as the charge compensation mechanism. In reality, once the external (ext) Mo is implanted in a lattice site, charge compensation must take place. As ion implantation is done at room temperature, ionic mobilities are very low, so it is likely that the charge compensation mechanism is electronic, specifically n-type and thus generating electrons. The energy band diagram, discussed subsequently, shows the probable

critical importance of the F<sup>+</sup> (V<sub>O</sub><sup>•</sup>) and the F<sup>++</sup> (V<sub>O</sub><sup>x</sup>) color centers, which derive from the intrinsic F<sup>0</sup> color centers (V<sub>O</sub><sup>••</sup>), as these facilitate n-type semiconductivity. The presence of these redox reactions and color centers is indicated in the PL data of Figure 3l, the peaks of which have previously been attributed to these features and the effects of which have been shown to be enhanced by Mo doping.<sup>57,58</sup> The same effect, albeit less intense, would occur with substitutional Mo solid solubility. To maintain charge balance, in the absence of O<sub>2</sub> (g), the oxygen vacancies must become neutrally charged and hence F<sup>++</sup> color centers.<sup>31</sup> For substitution, the defect equilibria are as follows:

Extrinsic



The discussion of the final column of Table 1 indicated that with interstitial solid solubility, the Mo<sup>6+</sup>/(Ce<sup>3+</sup> → Ce<sup>4+</sup>) ratio should be 1/6. The equilibria in eq 9 show that if substitutional solid solubility occurs, this ratio is 1/3. Consequently, this analysis supports the conclusion that the solid solubility mechanism is interstitial.

Row 4: The subsurface [O<sup>2-</sup>] values confirm the effect of reduction under N<sub>2</sub> and the partial reversal of the Ce reduction.

Row 5: Comparison of the corresponding data in rows 2 and 3 (assuming one oxygen bonded to one Ce<sup>3+</sup>) indicates that CeO<sub>2-x</sub> annealed in air has ~4 times as many subsurface Ce<sup>3+</sup> ions as on the surface, while CeO<sub>2-x</sub> annealed under N<sub>2</sub> has ~2 times as many. This shows that the reduction is not limited to the surface and hence also involves the subsurface.

Rows 6 and 7: These data are calculated on the assumption that two Ce<sup>3+</sup> are charge-compensated by one V<sub>O</sub><sup>••</sup> (eq 7). However, with Mo doping by ion implantation, this relation is invalid because the external Mo dopant addition is charge-compensated by the Ce<sup>3+</sup> ↔ Ce<sup>4+</sup> redox (eq 8), although the [V<sub>O</sub><sup>••</sup>] becomes [V<sub>O</sub><sup>x</sup>].

Row 8: The [Mo] solid solubility is ~1 atom %. It also supports the conclusion that V<sub>Ce</sub><sup>'''</sup> does not form for charge compensation from Mo substitutional or interstitial solid solubility.

Mo-CeO<sub>2-x</sub>/CeO<sub>2-x</sub> column: The final column in Table 1 examines the effect of simultaneous Ce<sup>4+</sup> reduction from annealing under N<sub>2</sub> and Ce<sup>3+</sup> oxidation from Mo ion implantation. These data show that this reversal ratio is

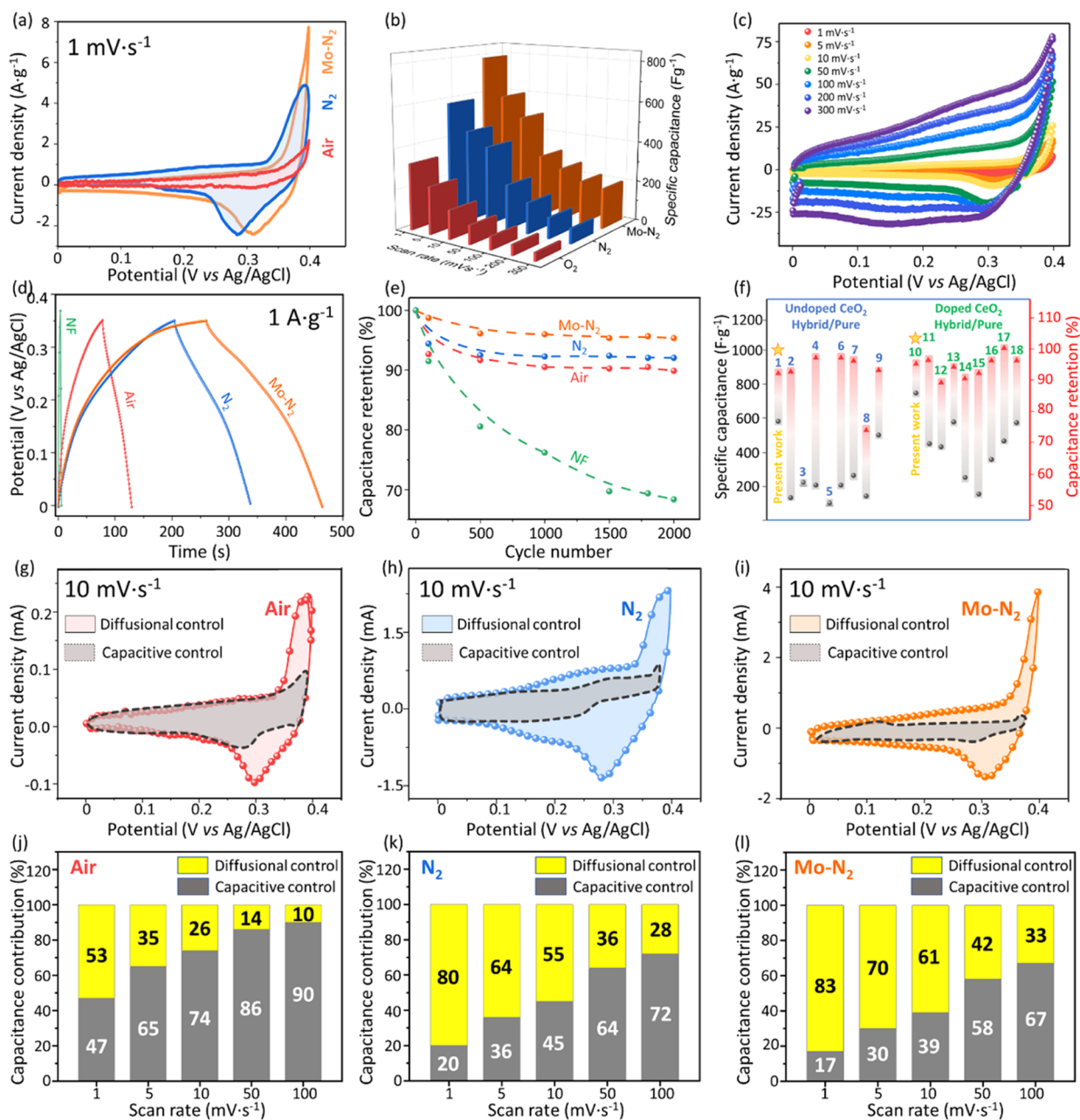


**Figure 4.** Electrochemical performance of  $\text{CeO}_{2-x}$ -based nanoflakes: (a) CV at  $1 \text{ mV s}^{-1}$ ; (b) specific capacitance at different scan rates for air,  $\text{N}_2$ , and  $\text{Mo-N}_2$ ; (c) CV curves of  $\text{Mo-N}_2$  at different scan rates; (d) galvanostatic charge/discharge curves at  $1 \text{ A g}^{-1}$ ; (e) stability performance up to 2000 cycles at  $100 \text{ mV s}^{-1}$ ; (f) comparison plot showing selected high specific capacitances of undoped and doped  $\text{CeO}_2$  in pure and hybrid pseudocapacitors in the present work (correspond to the data and references in Table S3); (g–i) deconvoluted data for diffusional and capacitive control at a scan rate of  $10 \text{ mV s}^{-1}$  based on CV: (g) air, (h)  $\text{N}_2$ , and (i)  $\text{Mo-N}_2$ ; and (j–l) deconvoluted data for diffusional and capacitive control as a function of scan rates ( $1\text{--}100 \text{ mV s}^{-1}$ ): (j) air, (k)  $\text{N}_2$ , and (l)  $\text{Mo-N}_2$ .

consistent at  $\sim 0.8$ , which suggests that  $\sim 20\%$  of the reduction is reversed by oxidation. This is very close to the expected ratio indicated in eq 8, which shows that one  $\text{Mo}^{6+}$  would cause six  $\text{Ce}^{3+} \rightarrow \text{Ce}^{4+}$  oxidations ( $\sim 17\%$ ). Although  $\text{Mo}^{5+}$  would give a closer match, the thermodynamic stability diagram indicates that  $\text{Mo}^{6+}$  should be the stable valence.

The electrochemical behavior of  $\text{CeO}_{2-x}$  nanoflakes was investigated in  $3 \text{ M NaOH}$  aqueous electrolyte using cyclic voltammetry and charge/discharge chronoamperometric methods. Figure 4a shows CV at the scan rate of  $1 \text{ mV s}^{-1}$  of  $\text{CeO}_{2-x}$  nanoflakes annealed in air or  $\text{N}_2$  and  $\text{CeO}_{2-x}$  nanoflakes ion-implanted with Mo and annealed under  $\text{N}_2$ .

Figure 4b confirms these comparative trends for CV at different scan rates. As the integrated CV area of a pattern divided by the scan rate represents the amount of gravimetric charge stored by the sample, the application of a reducing atmosphere during annealing increases the specific capacitance. The specific capacitances of air,  $\text{N}_2$ , and  $\text{Mo-N}_2$  calculated from these CV curves are  $328$ ,  $583$ , and  $764 \text{ F g}^{-1}$ , respectively.

It is notable that the value for  $\text{CeO}_{2-x}$  nanoflakes annealed in air is approximately half that annealed under  $\text{N}_2$  and, more importantly, the latter exhibit a specific capacitance that slightly exceeds the theoretical value of  $\text{CeO}_2$  of  $562 \text{ F g}^{-1}$ .<sup>18,23</sup> The enhancements in specific capacitance from Mo ion

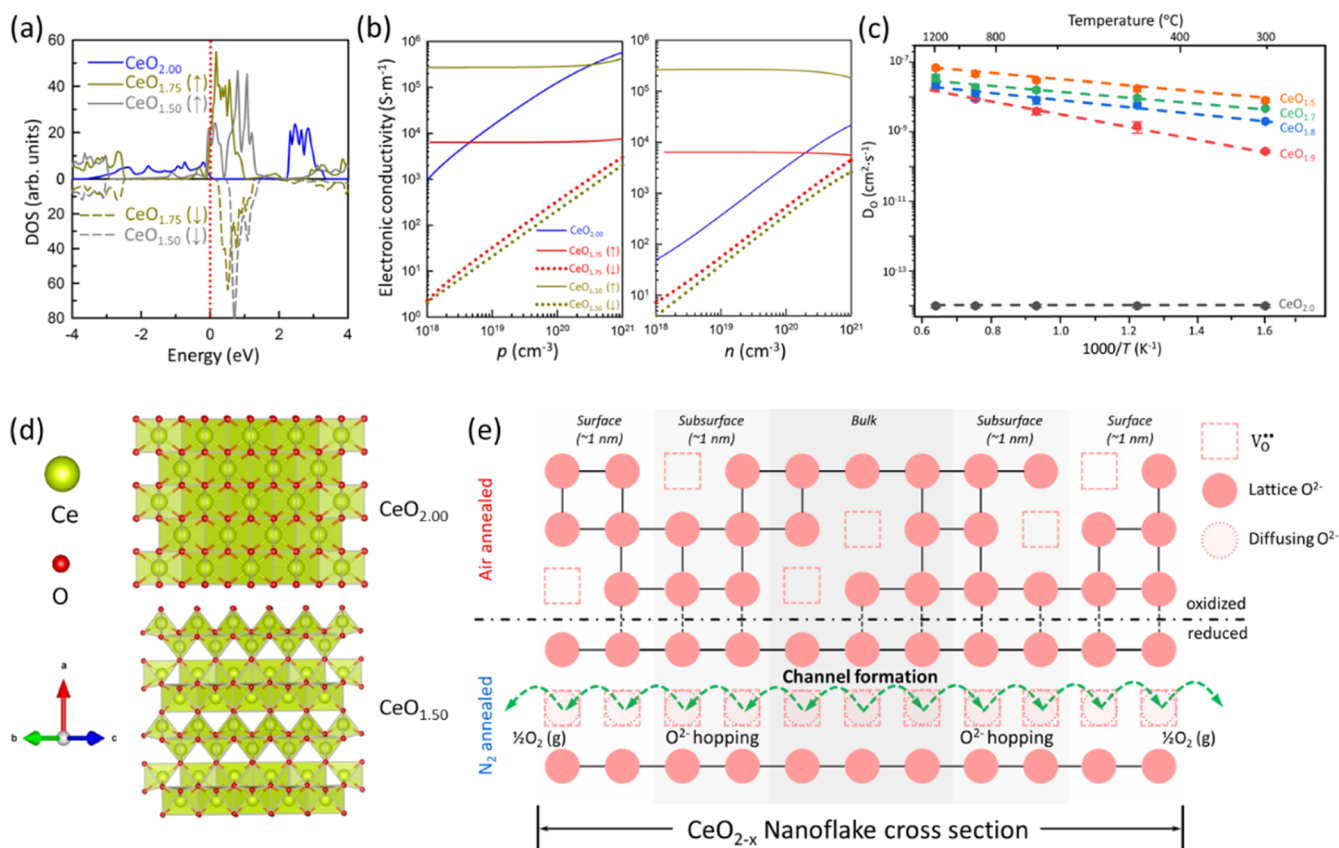


**Figure 5.** (a) Density of states of stoichiometric CeO<sub>2</sub> and nonstoichiometric CeO<sub>2-x</sub> calculated by DFT (the up and down arrows represent spin-up and spin-down electrons, and the red dotted line indicates the relative Fermi level); (b) electronic conductivities of CeO<sub>2</sub> and CeO<sub>2-x</sub> as a function of charge carrier density ( $p = p$ -type conductivity,  $n = n$ -type conductivity); (c) oxygen diffusion coefficients of CeO<sub>2</sub> and CeO<sub>2-x</sub> by classical molecular dynamics; (d) ball-and-stick representations of the ground-state geometries of CeO<sub>2</sub> and CeO<sub>2-x</sub> calculated by first-principles methods; and (e) schematic of oxygen vacancy channel non-formation and formation mechanisms of CeO<sub>2</sub> and CeO<sub>2-x</sub>, respectively.

implantation and from decreasing scan rate are confirmed in Figure 4b. The latter is indicative of the necessity of low scan rates ( $\leq 10 \text{ mV s}^{-1}$ ) in order to provide the electrolyte ions sufficient time to access active sites.<sup>59</sup> In contrast, the more rectangular shapes of the CV curves at high scan rates ( $\geq 200 \text{ mV s}^{-1}$ ), which avoid the generation of the redox peaks apparent in Figure 4c, are necessary to allow the electrolyte ions to undergo reversible absorption/desorption.<sup>59</sup>

In order to determine contribution to the CV data from Ni foam, galvanostatic charge/discharge curves of Ni foam and the three electrodes were obtained through chronoamperometric measurements at a constant current of  $1 \text{ A g}^{-1}$  within the potential window of 0 and 0.35 V versus Ag/AgCl, as shown in Figure 4d. It is very clear that the Ni foam has very short charging and discharging times compared to the three CeO<sub>2-x</sub> nanoflake samples, so it can be concluded that the effect of the former on the latter is negligible. Previous work has revealed that CeO<sub>2</sub>-based pseudocapacitors suffer from unbalanced rates of charging/discharging, where charging takes much longer than discharging.<sup>60</sup> This disadvantage can reduce both energy and power densities of such electrodes. However, the present work shows that the introduction of high  $[V_{O}^{\bullet\bullet}]$  and metal ion implantation have the capacity to resolve these issues. The data in Figure 4d show that the respective charge/discharge time ratios were 3.54, 1.56, and 1.33, thus indicating considerable improvement in balancing the two processes, especially for Mo-N<sub>2</sub>. As shown in Figure 4e, the capacitance retention was studied by applying CV at 2000 cycles at the

intermediate scan rate of  $100 \text{ mV s}^{-1}$ . The Ni foam shows the lowest stability with a  $>30\%$  decrease after 2000 cycles. In contrast, all three of the CeO<sub>2-x</sub>-based electrodes exhibit high stabilities, where Mo-N<sub>2</sub> has the highest stability at 95% retention and N<sub>2</sub> and air have 92 and 89%, respectively. Since the linear segment of the curve commences at 500 cycles (97% retention), these data suggest a lifetime of  $>70,000$  cycles. Figure 4b,d,e shows that Mo-N<sub>2</sub> exhibits the best performance in terms of gravimetric capacitance, the discharge period, and capacitance retention. Figure 4f compares the data for the gravimetric capacitance and capacitance retention for the present work in contrast with a range of other recent reports, which are summarized in Table S3. Furthermore, the electrochemical mechanisms were investigated by deconvolution of the CV data in Figure 4c using the Dunn method<sup>61,62</sup>

$$i = k_1 v + k_2 v^{1/2} \quad (10)$$

In eq 10,  $k_1$  is the slope,  $k_2$  is the ordinate intercept, and  $v$  is the scan rate. The capacitive control ( $k_1 v$ ) occurs at the surface, and the diffusional control ( $k_2 v^{1/2}$ ) occurs within the subsurface and bulk layers. Figure 4g-i shows capacitive and diffusion contributions in total capacitance of air, N<sub>2</sub>, and Mo-N<sub>2</sub> samples at a scan rate of  $10 \text{ mV s}^{-1}$ . The majority of the diffusion contribution in the N<sub>2</sub> and Mo-N<sub>2</sub> samples proves the major role of vacancies in the formation of intercalation-based reactions during the charge process. The complete data contrasting these two components of the electrochemical mechanisms are shown in Figure 4j-l. These data are

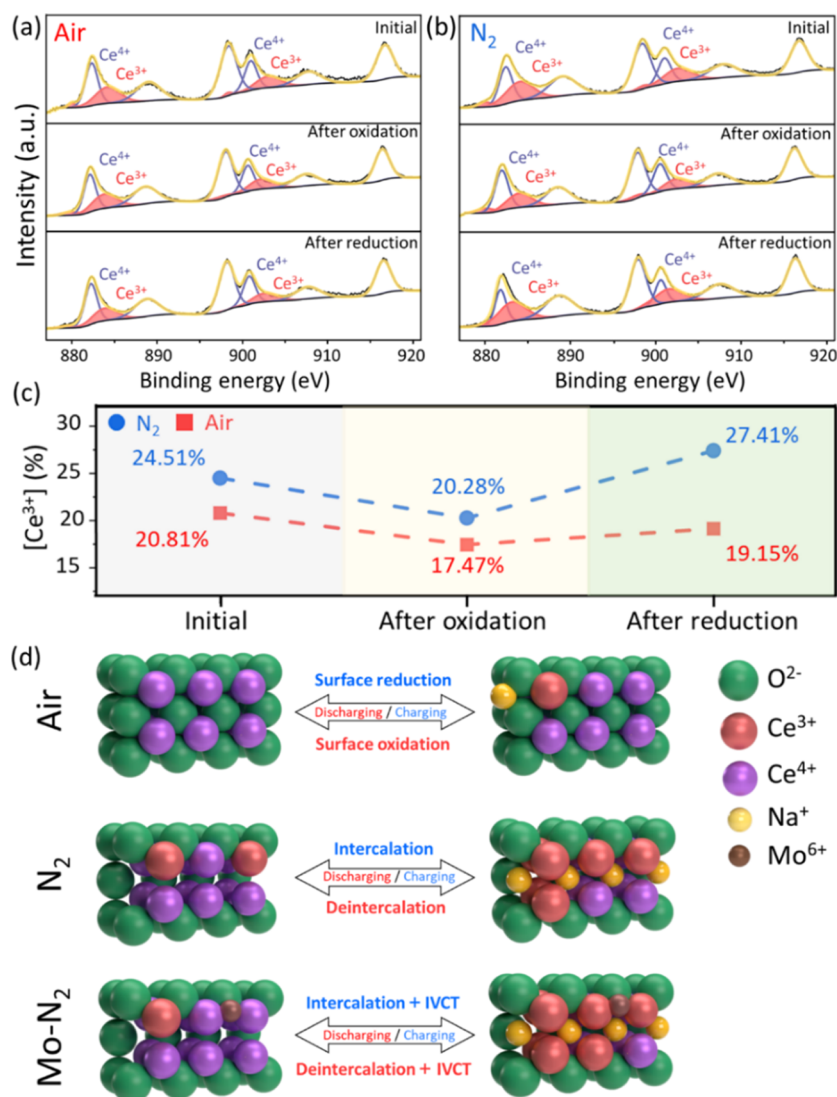


**Figure 6.** XPS Ce 3d spectra following charging reduction and discharging oxidation using CV at a scan rate of 5 mV/s and potential window of 0–0.4 V vs Ag/AgCl: (a) air; (b) N<sub>2</sub>; (c) comparative [Ce<sup>3+</sup>] data from Figure 6a,b; and (d) schematic of charging and discharging processes of air, N<sub>2</sub>, and Mo–N<sub>2</sub>.

unambiguous in revealing that diffusional control increases in the order air  $\ll$  N<sub>2</sub> < Mo–N<sub>2</sub>, so reduction plays a significant role in introducing intercalation capacitance. As these data decouple the effects of reduction (significant) and doping (less significant) on the performance, they suggest mutual contributions from these parameters on both the architectural design and the defect equilibria.

The similarity of the PL data in Figure 3l is significant in that it demonstrates that defects are not the governing factor in the recombination time. Since the common factor in these samples is the thickness, the recombination is dominated by the diffusion distance across the nanoflakes. The impact of this directionality was examined by spin-polarized density functional theory (DFT) calculations of the lifting of the electronic spin degeneracy from CeO<sub>2</sub> to CeO<sub>2–x</sub> (Figure 5a). While pristine CeO<sub>2,00</sub> has a magnetic moment of 0 and so is non-magnetic, CeO<sub>1,75</sub> and CeO<sub>1,50</sub> exhibit net magnetic moments of 0.5 and 1.0  $\mu$ B per formula unit, respectively. These finite magnetic moments are associated with conducting electrons as shown in Figure 5a. At the same time, the band gaps of these two samples are impacted significantly. The DFT calculations

based on the TB-mBJ exchange–correlation functional yield a band gap for pristine CeO<sub>2,00</sub> of 2.3 eV, which increased to 3.0 eV for CeO<sub>1,75</sub> and 3.1 eV for CeO<sub>1,50</sub>. The calculated band gaps of the latter two are reduced for spin up and increased for spin down. Furthermore, the Fermi energy level (red dotted line) is shifted relatively from the top of the valence band for pristine CeO<sub>2,00</sub> to the bottom of the conduction band for both CeO<sub>1,75</sub> and CeO<sub>1,50</sub>. Thus, stoichiometric p-type CeO<sub>2,00</sub> can be converted to n-type CeO<sub>2–x</sub> through the introduction of oxygen vacancies, which are charge-compensated by Ce<sup>4+</sup>  $\rightarrow$  Ce<sup>3+</sup> redox, thereby introducing a magnetic moment. Boltzmann transport calculations based on the DFT calculation indicate that the electronic conductivity associated with a magnetic moment increases several orders of magnitude with increasing [V<sub>O</sub><sup>••</sup>] at typical charge carrier concentrations of  $\leq 10^{20}$  e<sup>–</sup> per cm<sup>3</sup> (Figure 5b).<sup>63</sup> Furthermore, if holes are the main charge carriers, the electrical conductivity behaves analogously but only for carrier concentrations of  $\leq 10^{18}$  h per cm<sup>3</sup>, that is, n-type conductivity is likely to be significantly higher than p-type conductivity at higher charge carrier concentrations. These results show explicitly that the

capacitance of CeO<sub>2</sub>-based materials can be improved by reduction, which enhances the [Ce<sup>3+</sup>] and alters p-type conductivity to n-type conductivity, and the formation of charge-compensating oxygen vacancies, which enhance electron conductivity.

For Mo-doped CeO<sub>2</sub>, midgap state energy ranges from intrinsic and extrinsic defects for substitutional and interstitial defects of the three Mo valences, calculated by spin-polarized DFT calculation, are shown in Figure S15. These simulations reveal that interstitial Mo<sup>5+</sup> and Mo<sup>6+</sup> generate shallow acceptor midgap states close to the valence band.<sup>64</sup> These have the capacity to result in free hole charge carriers, but interstitial Mo<sup>4+</sup> and Mo<sup>5+</sup> also generate deep trapping states, which can act as recombination centers.

In contrast, Mo<sup>4+</sup> and the color centers F<sup>++</sup> (V<sub>O</sub><sup>x</sup>) and F<sup>+</sup> (VO<sup>•</sup>) generate intrinsic shallow donor midgap states close to the conduction band. These have the capacity to result in free electron charge carriers. Interestingly, these simulations indicate that the F<sup>0</sup> color center (V<sub>O</sub><sup>••</sup>), that is, an oxygen vacancy, is unimportant, as it corresponds to the conduction band minimum (CBM). Ultimately, these data reveal that the F<sup>+</sup> and possibly the F<sup>++</sup> color centers enable n-type semiconductivity and that Mo doping itself serves only to facilitate the probable formation of the color centers. The preceding data allowed DFT examination of the energies associated with different configurations for the distribution of oxygen vacancies. These calculations indicated that the lowest energy was associated with the maximal possible [V<sub>O</sub><sup>••</sup>], viz., CeO<sub>1.50</sub>. More importantly, the data in Figure 5d show that the oxygen vacancies are ordered into channels of orthogonal orientation. Figure 5e shows how surface reduction can initiate formation of an oxygen vacancy and that directional oxygen diffusivity can result in channel formation across with thickness of the nanoflake.

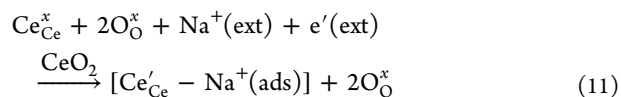
However, Figure 2h shows that the nanoflakes are randomly oriented polycrystals, without clear indication of the presence of discrete crystallite or grain boundaries. Consequently, the channels between the parallel surfaces of the nanoflakes must be variably oriented, as the crystallites are randomly oriented. Since these channels are lined with Ce<sup>3+</sup>, the extra electron establishes a negatively charged channel that facilitates the transport of electrons and the trapping of holes. Since the PL data indicate similar recombination times for the nanoflakes, either the differences between the PL data are indicative of the different channel lengths or the charge carrier speed is sufficiently high to obscure any detectable path length differences.

The presence of these oxygen vacancy channels from reduction has a critical effect on the surface and intercalation capacitances because they are both large-scale electron traps and volumes for cation intercalation. Furthermore, the data in Table 1 and eq 8 show that ion implantation of Mo results in partial elimination of the [Ce<sup>3+</sup>]. As the ion implantation is likely to be concentrated on the surfaces of the nanoflakes, the localized reduction in the number of Ce<sup>3+</sup> ions would not result in the annihilation of V<sub>O</sub><sup>••</sup> but in their conversion to V<sub>O</sub><sup>x</sup> and VO<sup>•</sup>. Consequently, this would reduce the repulsion between the electrolyte cations and the oxygen vacancies, thereby enhancing intercalation.

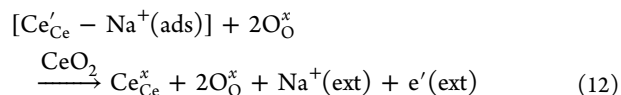
In pseudocapacitors, the charging (reduction) and discharging (oxidation) processes are based on transitions between the valence states of metal ions of the relevant electrode,<sup>13</sup> where a low redox potential would facilitate this switching and

associated reversibility. Figure 6a–c shows the effects of these intrinsic processes on the [Ce<sup>3+</sup>] of CeO<sub>2-x</sub> and reveals the importance of the formation of the oxygen vacancy channels, that is, the nanoflakes annealed in air lacked the driving force for oxygen vacancy channel formation, so the initial [Ce<sup>3+</sup>] was low (20.81%) and reduction charging reduced the [Ce<sup>3+</sup>]. Alternatively, oxidation charging only partially returns the [Ce<sup>3+</sup>] to its previous level (19.15%). In contrast, the nanoflakes annealed in air, which contain oxygen vacancy channels initiated and grown during annealing under N<sub>2</sub>, show a higher initial [Ce<sup>3+</sup>] (24.51%), a similar reduced [Ce<sup>3+</sup>] upon oxidation discharging, but an increase upon reduction charging in [Ce<sup>3+</sup>] to a level greater than that initially present (27.41%). These indicate that the presence of the oxygen vacancy channels allows ~35% of the Ce<sup>3+</sup> to participate in redox, while the absence of the channels allows only ~10% of the Ce<sup>3+</sup> to participate. This difference suggests that ~10% of the pseudocapacitance derives from the surface but ~25% derives from the bulk, thereby demonstrating simultaneous surface and bulk intercalation pseudocapacitance. A schematic diagram of these charging and discharging processes is shown in Figure 6d. For CeO<sub>2-x</sub>, the electrochemical defect equilibria, which describe charge/discharge, illustrate that Ce<sup>3+</sup> is the active site for Na<sup>+</sup> adsorption:

Reduction charging

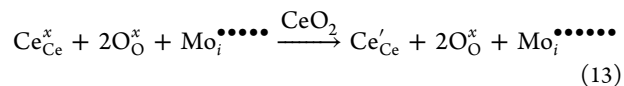


Oxidation discharging

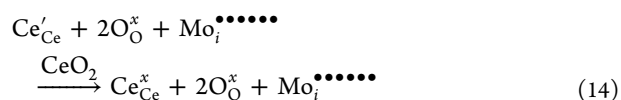


The Na<sup>+</sup>(ext) indicates Na<sup>+</sup> supplied externally as an electrolyte, e' (ext) indicates electron supplied externally by power, and [Ce'<sub>Ce</sub>–Na<sup>+</sup>(ads)] indicates Na<sup>+</sup> adsorbed on Ce<sup>3+</sup>. For Mo ion-implanted CeO<sub>2-x</sub>, the superior pseudocapacitive performances are likely derived from the effect of Mo redox linked to Ce redox through IVCT:

Reduction charging



Oxidation discharging



Consequently, IVCT provides a second driving force for Ce<sup>3+</sup> switching in addition to the electrochemical redox reactions, where the direction depends on charging versus discharging and the extent depends on the dopant level. Since ion implantation is likely to concentrate Mo on the surfaces, its effects would be amplified, thus increasing the impact of IVCT.

More broadly, this observation suggests the advantage of decorating surfaces with Mo using other techniques that are less complex than ion implantation, such as simple surface precipitation from a suspension during drying followed by annealing.

Finally, while eqs 11 and 12 indicate that  $\text{Ce}^{4+} \rightarrow \text{Ce}^{3+}$  is an intrinsic process through defect equilibration for pure  $\text{CeO}_{2-x}$ , eqs 13 and 14 indicate that this is an extrinsic process through IVCT for Mo ion-implanted  $\text{CeO}_{2-x}$ .

XPS data combined with defect equilibria are emerging as powerful tools in the interpretation of mechanistic redox phenomena imposed by doping and/or atmospheric treatment and their effects on semiconducting properties in energy transformation.<sup>31,65,66</sup> However, the PL data in the present work allow the applicability of this tool to be raised to a new level by applying this approach to charge/discharge phenomena imposed by electrochemistry and their effects on the capacitive properties in energy storage.

### 3. CONCLUSIONS

The present work strategizes defect engineering and architectural design to demonstrate for the first time intercalation pseudocapacitance from dense-packing cubic  $\text{CeO}_{2-x}$ . The fabrication process leverages a precision template-free electrochemical deposition technique to form  $\text{CeO}_{2-x}$  nanoflakes on Ni foam substrates, followed by low-energy Mo ion implantation and low-temperature reduction.

Initially, the  $\text{CeO}_{2-x}$  is charge-balanced through  $\text{Ce}^{4+} \rightarrow \text{Ce}^{3+}$  reduction and ionic charge compensation through  $\text{V}_{\text{O}}^{\bullet\bullet}$  formation. The ion-implanted Mo acts as a donor dopant in the interstitial position, which results in  $\text{Ce}^{3+} \rightarrow \text{Ce}^{4+}$  oxidation. Critically, the introduction of Mo into the lattice results in two forms of electronic charge compensation, which are affected by the conversion of the intrinsic ( $\text{F}^0$  color centers ( $\text{V}_{\text{O}}^{\bullet\bullet}$ ) to  $\text{F}^+$  ( $\text{V}_{\text{O}}^{\bullet}$ ) and  $\text{F}^{++}$  ( $\text{V}_{\text{O}}^{\bullet\bullet}$ ) color centers and, more critically, the generation of electrons, which enables n-type semiconductivity, that is, the principal role of the ion-implanted  $\text{Mo}^{6+}$  is not specifically the alteration of the energy band diagram but in facilitating the generation of electrons and to establish the midgap states for  $\text{V}_{\text{O}}^{\bullet}$  and  $\text{V}_{\text{O}}^{\bullet\bullet}$ , which facilitate their transfer across the band gap.

The solid solubility mechanism and charge compensation mechanisms combined with critical PL recombination times revealed that the dominant effect is not provided through the latter but through the consistent thicknesses of the nanoflakes. This essential observation is validated by the DFT simulations, the mechanism of which shows that surface reduction leads to the progressive formation of ordered oxygen vacancy channels. These channels effectively act as prolific and stable active sites for adsorption sites for electrolyte ions. The dominance of the diffusional electrochemical mechanism derives largely from the reduction, which formed these channels, rather than the Mo doping.

Consequently, the presence of oxygen vacancy channels in  $\text{CeO}_{2-x}$  nanoflakes endow the capacity of the surface and intercalation pseudocapacitance, thus improving its capacitance. Also, these channels are more stable and offer significantly higher numbers of active sites and significantly greater access to them compared to randomly distributed oxygen vacancies. During the charging/discharging process, the surface redox is responsible for  $\sim 10$  atom % of the  $\text{Ce}^{3+}$  and intercalation redox is responsible for  $\sim 25\%$  of the  $\text{Ce}^{3+}$ .

The present work offers a feasible way to functionalize intercalation pseudocapacitance by decoupling the working mechanism of oxygen vacancies and donor doping in electrochemical application, and this work offers the mechanistic analyses of defect engineering and architectural design for further exploration of pseudocapacitive behavior.

## ■ ASSOCIATED CONTENT

### Supporting Information

The Supporting Information is available free of charge at <https://pubs.acs.org/doi/10.1021/acsami.1c14484>.

FTIR, EDS, SEM, XRD, PIXE, Pourbaix diagram, stability diagram, Raman, energy level diagram, defect equilibria, lattice parameters, and summary of work on supercapacitors (PDF)

## ■ AUTHOR INFORMATION

### Corresponding Authors

Xiaoran Zheng – School of Materials Science and Engineering, University of New South Wales, Sydney, New South Wales 2052, Australia; [orcid.org/0000-0002-7016-5260](https://orcid.org/0000-0002-7016-5260);  
Email: [xiaoran.zheng@unsw.edu.au](mailto:xiaoran.zheng@unsw.edu.au)

Sajjad S. Mofarah – School of Materials Science and Engineering, University of New South Wales, Sydney, New South Wales 2052, Australia; [orcid.org/0000-0002-4835-767X](https://orcid.org/0000-0002-4835-767X); Email: [s.seifimofarah@unsw.edu.au](mailto:s.seifimofarah@unsw.edu.au)

Pramod Koshy – School of Materials Science and Engineering, University of New South Wales, Sydney, New South Wales 2052, Australia; Email: [koshy@unsw.edu.au](mailto:koshy@unsw.edu.au)

### Authors

Alan Cen – School of Materials Science and Engineering, University of New South Wales, Sydney, New South Wales 2052, Australia

Claudio Cazorla – School of Materials Science and Engineering, University of New South Wales, Sydney, New South Wales 2052, Australia; Present Address: Departament de Física, Universitat Politècnica de Catalunya, Campus Nord B4-B5, Barcelona 08034, Spain

Enamul Haque – EH Solid State Physics Laboratory, Gaffargaon, Mymensingh 2233, Bangladesh; [orcid.org/0000-0002-5291-7203](https://orcid.org/0000-0002-5291-7203)

Ewing Y. Chen – School of Materials Science and Engineering, University of New South Wales, Sydney, New South Wales 2052, Australia

Armand J. Atanacio – Centre for Accelerator Science, Australian Nuclear Science and Technology Organisation, Lucas Heights, New South Wales 2234, Australia

Madhura Manohar – Centre for Accelerator Science, Australian Nuclear Science and Technology Organisation, Lucas Heights, New South Wales 2234, Australia

Corey Vutukuri – School of Materials Science and Engineering, University of New South Wales, Sydney, New South Wales 2052, Australia

Joel Luke Abraham – School of Materials Science and Engineering, University of New South Wales, Sydney, New South Wales 2052, Australia

Charles C. Sorrell – School of Materials Science and Engineering, University of New South Wales, Sydney, New South Wales 2052, Australia

Complete contact information is available at: <https://pubs.acs.org/doi/10.1021/acsami.1c14484>

### Author Contributions

X.Z. undertook experimental work, conducted characterization and data analysis, wrote the initial draft of the article, and worked on all subsequent drafts. S.S.M. designed the experimental program, worked on all subsequent drafts, and

supervised the project. A.C. undertook the electrochemical and characterization testing and wrote the associated preliminary data analysis, C.C. and E.H. undertook all of the DFT work, wrote the associated data analysis, and contributed to the final draft, E.Y.C. assisted with experiment and worked on all subsequent drafts, A.J.A. and M.M. undertook ion implantation work, and C.V. and J.L.A. provided technical support during the revision of the manuscript. P.K. jointly supervised the project and worked on all subsequent drafts. C.C.S. jointly supervised the project, provided the basis for the formal data analysis, and worked on all subsequent drafts.

## Notes

The authors declare no competing financial interest.

## ACKNOWLEDGMENTS

The authors acknowledge financial support from the Australian Research Council (ARC Grant DP170104130) and the characterization facilities provided by the Mark Wainwright Analytical Centre at UNSW Sydney. The authors acknowledge the support of the Australian Government in provision of access to the ion implantation capabilities at the Australian Nuclear Science Technology Organisation's Centre for Accelerator Science, which is also partly funded through Australia's National Collaborative Research Infrastructure Strategy.

## REFERENCES

- (1) Raza, W.; Ali, F.; Raza, N.; Luo, Y.; Kim, K.-H.; Yang, J.; Kumar, S.; Mehmood, A.; Kwon, E. E. Recent Advancements in Supercapacitor Technology. *Nano Energy* **2018**, *52*, 441–473.
- (2) Wang, G.; Zhang, L.; Zhang, J. A Review of Electrode Materials for Electrochemical Supercapacitors. *Chem. Soc. Rev.* **2012**, *41*, 797–828.
- (3) Chodankar, N. R.; Pham, H. D.; Nanjundan, A. K.; Fernando, J. F. S.; Jayaramulu, K.; Golberg, D.; Han, Y. K.; Dubal, D. P. True Meaning of Pseudocapacitors and Their Performance Metrics: Asymmetric versus Hybrid Supercapacitors. *Small* **2020**, *16*, 2002806.
- (4) Hu, C.-C.; Chang, K.-H.; Lin, M.-C.; Wu, Y.-T. Design and Tailoring of the Nanotubular Arrayed Architecture of Hydrrous RuO<sub>2</sub> for Next Generation Supercapacitors. *Nano Lett.* **2006**, *6*, 2690–2695.
- (5) Liu, T.; Pell, W. G.; Conway, B. E. Self-Discharge and Potential Recovery Phenomena at Thermally and Electrochemically Prepared RuO<sub>2</sub> Supercapacitor Electrodes. *Electrochim. Acta* **1997**, *42*, 3541–3552.
- (6) Yu, Z.; Duong, B.; Abbitt, D.; Thomas, J. Highly Ordered MnO<sub>2</sub> Nanopillars for Enhanced Supercapacitor Performance. *Adv. Mater.* **2013**, *25*, 3302–3306.
- (7) Subramanian, V.; Zhu, H.; Wei, B. Nanostructured MnO<sub>2</sub>: Hydrothermal Synthesis and Electrochemical Properties as A Supercapacitor Electrode Material. *J. Power Sources* **2006**, *159*, 361–364.
- (8) Shivakumara, S.; Penki, T. R.; Munichandraiah, N. High Specific Surface Area  $\alpha$ -Fe<sub>2</sub>O<sub>3</sub> Nanostructures as High Performance Electrode Material for Supercapacitors. *Mater. Lett.* **2014**, *131*, 100–103.
- (9) Jiang, Q.; Kurra, N.; Alhabeab, M.; Gogotsi, Y.; Alshareef, H. N. All Pseudocapacitive MXene-RuO<sub>2</sub> Asymmetric Supercapacitors. *Adv. Energy Mater.* **2018**, *8*, 1703043.
- (10) Chen, S.; Zhu, J.; Wu, X.; Han, Q.; Wang, X. Graphene Oxide-MnO<sub>2</sub> Nanocomposites for Supercapacitors. *ACS Nano* **2010**, *4*, 2822–2830.
- (11) Chen, Z.; Augustyn, V.; Wen, J.; Zhang, Y.; Shen, M.; Dunn, B.; Lu, Y. High-Performance Supercapacitors Based on Intertwined CNT/V<sub>2</sub>O<sub>5</sub> Nanowire Nanocomposites. *Adv. Mater.* **2011**, *23*, 791–795.
- (12) Bi, W.; Wang, J.; Jahrman, E. P.; Seidler, G. T.; Gao, G.; Wu, G.; Cao, G. Interface Engineering V<sub>2</sub>O<sub>5</sub> Nanofibers for High-Energy and Durable Supercapacitors. *Small* **2019**, *15*, 1901747.
- (13) Kim, H.-S.; Cook, J. B.; Lin, H.; Ko, J. S.; Tolbert, S. H.; Ozolins, V.; Dunn, B. Oxygen Vacancies Enhance Pseudocapacitive Charge Storage Properties of MoO<sub>3-x</sub>. *Nat. Mater.* **2017**, *16*, 454–460.
- (14) Ambade, S. B.; Ambade, R. B.; Eom, W.; Noh, S. H.; Kim, S. H.; Han, T. H. 2D Ti<sub>3</sub>C<sub>2</sub> MXene/WO<sub>3</sub> Hybrid Architectures for High-Rate Supercapacitors. *Adv. Mater. Interfaces* **2018**, *5*, 1801361.
- (15) Wang, X.; Li, G.; Chen, Z.; Augustyn, V.; Ma, X.; Wang, G.; Dunn, B.; Lu, Y. High-Performance Supercapacitors Based on Nanocomposites of Nb<sub>2</sub>O<sub>5</sub> Nanocrystals and Carbon Nanotubes. *Adv. Energy Mater.* **2011**, *1*, 1089–1093.
- (16) Poudel, M. B.; Yu, C.; Kim, H. J. Synthesis of Conducting Bifunctional Polyaniline@Mn-TiO<sub>2</sub> Nanocomposites for Supercapacitor Electrode and Visible Light Driven Photocatalysis. *Catalysts* **2020**, *10*, 546–756.
- (17) Mofarah, S. S.; Adabifiroozjaei, E.; Pardehkhorrarn, R.; Assadi, M. H. N.; Hinterstein, M.; Yao, Y.; Liu, X.; Ghasemian, M. B.; Kalantar-Zadeh, K.; Mehmood, R.; Cazorla, C.; Shahmiri, R.; Bahmanrokh, G.; Bhattacharyya, S.; Spadaro, M. C.; Arbiol, J.; Lim, S.; Xu, Y.; Arandiyana, H.; Scott, J.; Koshy, P.; Sorrell, C. C. Coordination Polymer to Atomically Thin, Holey, Metal-Oxide Nanosheets for Tuning Band Alignment. *Adv. Mater.* **2019**, *31*, 1905288.
- (18) Maiti, S.; Pramanik, A.; Mahanty, S. Extraordinarily High Pseudocapacitance of Metal Organic Framework Derived Nanostructured Cerium Oxide. *Chem. Commun.* **2014**, *50*, 11717–11720.
- (19) Maheswari, N.; Muralidharan, G. Hexagonal CeO<sub>2</sub> Nanostructures: An Efficient Electrode Material for Supercapacitors. *Dalton Trans.* **2016**, *45*, 14352–14362.
- (20) Govindan, R.; Hong, X.-J.; Sathishkumar, P.; Cai, Y.-P.; Gu, F. L. Construction of Metal-Organic Framework-Derived CeO<sub>2</sub>/C Integrated MoS<sub>2</sub> Hybrid for High-Performance Asymmetric Supercapacitor. *Electrochim. Acta* **2020**, *353*, 136502.
- (21) Leong, Z. Y.; Yang, H. Y. A Study of MnO<sub>2</sub> with Different Crystalline Forms for Pseudocapacitive Desalination. *ACS Appl. Mater. Interfaces* **2019**, *11*, 13176–13184.
- (22) Zhu, Y.-P.; Xia, C.; Lei, Y.; Singh, N.; Schwingenschlöggl, U.; Alshareef, H. N. Solubility Contrast Strategy for Enhancing Intercalation Pseudocapacitance in Layered MnO<sub>2</sub> Electrodes. *Nano Energy* **2019**, *56*, 357–364.
- (23) Mofarah, S. S.; Adabifiroozjaei, E.; Yao, Y.; Koshy, P.; Lim, S.; Webster, R.; Liu, X.; Khayyam Nekouei, R.; Cazorla, C.; Liu, Z.; Wang, Y.; Lambropoulos, N.; Sorrell, C. C. Proton-Assisted Creation of Controllable Volumetric Oxygen Vacancies in Ultrathin CeO<sub>2-x</sub> for Pseudocapacitive Energy Storage Applications. *Nat. Commun.* **2019**, *10*, 2594.
- (24) Zhang, W.; Cai, L.; Cao, S.; Qiao, L.; Zeng, Y.; Zhu, Z.; Lv, Z.; Xia, H.; Zhong, L.; Zhang, H.; Ge, X.; Wei, J.; Xi, S.; Du, Y.; Li, S.; Chen, X. Interfacial Lattice-Strain-Driven Generation of Oxygen Vacancies in An Aerobic-Annealed TiO<sub>2</sub>(B) Electrode. *Adv. Mater.* **2019**, *31*, 1906156.
- (25) Yang, C.; Lu, Y.; Zhang, L.; Kong, Z.; Yang, T.; Tao, L.; Zou, Y.; Wang, S. Defect Engineering on CeO<sub>2</sub>-Based Catalysts for Heterogeneous Catalytic Applications. *Small Struct.* **2021**, 2100058.
- (26) Xie, C.; Yan, D.; Li, H.; Du, S.; Chen, W.; Wang, Y.; Zou, Y.; Chen, R.; Wang, S. Defect Chemistry in Heterogeneous Catalysis: Recognition, Understanding, and Utilization. *ACS Catal.* **2020**, *10*, 11082–11098.
- (27) Xiao, Z.; Huang, Y.-C.; Dong, C.-L.; Xie, C.; Liu, Z.; Du, S.; Chen, W.; Yan, D.; Tao, L.; Shu, Z.; Zhang, G.; Duan, H.; Wang, Y.; Zou, Y.; Chen, R.; Wang, S. Operating Identification of the Dynamic Behavior of Oxygen Vacancy-Rich Co<sub>3</sub>O<sub>4</sub> for Oxygen Evolution Reaction. *J. Am. Chem. Soc.* **2020**, *142*, 12087–12095.
- (28) Gao, P.; Chen, Z.; Gong, Y.; Zhang, R.; Liu, H.; Tang, P.; Chen, X.; Passerini, S.; Liu, J. The Role of Cation Vacancies in Electrode Materials for Enhanced Electrochemical Energy Storage:

Synthesis, Advanced Characterization, and Fundamentals. *Adv. Energy Mater.* **2020**, *10*, 1903780.

(29) Yan, D.; Li, Y.; Huo, J.; Chen, R.; Dai, L.; Wang, S. Defect Chemistry of Nonprecious-Metal Electrocatalysts for Oxygen Reactions. *Adv. Mater.* **2017**, *29*, 1606459.

(30) Lu, Y.; Liu, T.; Dong, C. L.; Huang, Y. C.; Li, Y.; Chen, J.; Zou, Y.; Wang, S. Tuning the Selective Adsorption Site of Biomass on  $\text{Co}_3\text{O}_4$  by Ir Single Atoms for Electrosynthesis. *Adv. Mater.* **2021**, *33*, 2007056.

(31) Xu, Y.; Mofarah, S. S.; Mehmood, R.; Cazorla, C.; Koshy, P.; Sorrell, C. C. Design Strategies for Ceria Nanomaterials: Untangling Key Mechanistic Concepts. *Mater. Horiz.* **2021**, *8*, 102–123.

(32) Mofarah, S. S.; Adabifiroozjahi, E.; Wang, Y.; Arandiyani, H.; Pardehkhorrani, R.; Yao, Y.; Assadi, M. H. N.; Mehmood, R.; Chen, W.-F.; Tsounis, C.; Scott, J.; Lim, S.; Webster, R.; Zhong, V.; Xu, Y.; Koshy, P.; Sorrell, C. C. Assembly of Cerium-Based Coordination Polymer into Variant Polycrystalline 2D-3D  $\text{CeO}_{2-x}$  Nanostructures. *J. Mater. Chem. A* **2020**, *8*, 4753–4763.

(33) Ni, B.; Wang, X. Face the Edges: Catalytic Active Sites of Nanomaterials. *Adv. Sci.* **2015**, *2*, 1500085.

(34) Huang, L.-F.; Hutchison, M. J.; Santucci, R. J., Jr; Scully, J. R.; Rondinelli, J. M. Improved Electrochemical Phase Diagrams from Theory and Experiment: The Ni–Water System and Its Complex Compounds. *J. Phys. Chem. C* **2017**, *121*, 9782–9789.

(35) Barnard, R.; Randell, C. F. Studies Concerning Charged Nickel Hydroxide Electrodes VIII the Relative Potentials of the  $\beta$ -/ $\gamma$ -Nickel Oxy Hydroxide Reduction Processes. *J. Appl. Electrochem.* **1983**, *13*, 97–101.

(36) Ghazaleh, A.; Aminayi, P.; Tasirin, S. M. Structural Properties and Optical Characterization of Flower-Like Mg Doped NiO. *AIP Adv.* **2015**, *5*, 077161.

(37) Fardood, T. S.; Ramazani, A.; Moradi, S. A Novel Green Synthesis of Nickel Oxide Nanoparticles Using Arabic Gum. *Chem. J. Mold.* **2017**, *12*, 115–118.

(38) Khairnar, D. S.; Shrivastava, V. S. Facile Synthesis of Nickel Oxide Nanoparticles for the Degradation of Methylene Blue and Rhodamine B Dye: A Comparative Study. *J. Taibah Univ. Sci.* **2019**, *13*, 1108–1118.

(39) Zeng, Y.; Priest, C.; Wang, G.; Wu, G. Restoring the Nitrogen Cycle by Electrochemical Reduction of Nitrate: Progress and Prospects. *Small Methods* **2020**, *4*, 2000672.

(40) Kröger, F.A.; Vink, H. J. Relations between the Concentrations of Imperfections in Crystalline Solids. *Solid State Phys.* **1956**, *3*, 307–435.

(41) Haynes, W. M. *CRC Handbook of Chemistry and Physics*; CRC Press: New York, USA, 2014.

(42) Ustinov, O.A.; Novoselov, G.; Andrianov, M.; Chebotarev, N. The  $\text{MoO}_3$ - $\text{CeO}_2$  System. *Zhurnal Neorganicheskoy Khimii* **1970**, *15*, 2549–2550.

(43) West, A. R. *Solid State Chemistry and Its Applications*; John Wiley & Sons: Oxford, U.K., 2014.

(44) Goldstein, J. I.; Newbury, D. E.; Michael, J. R.; Ritchie, W. M.; Henry, J.; Scott, J.; David, C. *Scanning Electron Microscopy and X-ray Microanalysis*; Springer: New York, USA, 2017.

(45) Kawashima, K.; Liu, Y.; Kim, J.-H.; Wygant, B. R.; Cheng, L.; Celio, H.; Mabayoje, O.; Lin, J.; Mullins, C. B. Infrared Light-Driven  $\text{LaW}(\text{O},\text{N})_3$  OER Photoelectrocatalysts from Chloride Flux-Grown  $\text{La}_4\text{W}_3\text{O}_{15}$  Templating Precursors. *ACS Appl. Energy Mater.* **2018**, *2*, 913–922.

(46) Vila, M.; Díaz-Guerra, C.; Lorenz, K.; Piqueras, J.; Piš, I.; Magnano, E.; Munuera, C.; Alves, E.; García-Hernández, M. Effects of Thermal Annealing on the Structural and Electronic Properties of Rare Earth-Implanted  $\text{MoO}_3$  Nanoplates. *CrystEngComm* **2017**, *19*, 2339–2348.

(47) Shannon, R. D.; Prewitt, C. T. Effective Ionic Radii in Oxides and Fluorides. *Acta Crystallogr., Sect. B: Struct. Sci., Cryst. Eng. Mater.* **1969**, *25*, 925–946.

(48) Sartoretti, E.; Novara, C.; Giorgis, F.; Piumetti, M.; Bensaid, S.; Russo, N.; Fino, D. In Situ Raman Analyses of the Soot Oxidation

Reaction over Nanostructured Ceria-Based Catalysts. *Sci. Rep.* **2019**, *9*, 3875.

(49) Mofarah, S. S.; Schreck, L.; Cazorla, C.; Zheng, X.; Adabifiroozjahi, E.; Tsounis, C.; Scott, J.; Shahmiri, R.; Yao, Y.; Abbasi, R.; Wang, Y.; Arandiyani, H.; Sheppard, L.; Wong, V.; Doustkhah, E.; Koshy, P.; Sorrell, C. C. Highly Catalytically Active  $\text{CeO}_{2-x}$ -Based Heterojunction Nanostructures with Mixed Micro/Meso-Porous Architectures. *Nanoscale* **2021**, *13*, 6764–6771.

(50) Natile, M. M.; Glisenti, A. Nanostructured  $\text{CeO}_2$  Powders by XPS. *Surf. Sci. Spectra* **2006**, *13*, 17–30.

(51) Wang, L.; Yu, Y.; He, H.; Zhang, Y.; Qin, X.; Wang, B. Oxygen Vacancy Clusters Essential for the Catalytic Activity of  $\text{CeO}_2$  Nanocubes for O-Xylene Oxidation. *Sci. Rep.* **2017**, *7*, 12845.

(52) Liu, Y.; Ma, C.; Zhang, Q.; Wang, W.; Pan, P.; Gu, L.; Xu, D.; Bao, J.; Dai, Z. 2D Electron Gas and Oxygen Vacancy Induced High Oxygen Evolution Performances for Advanced  $\text{Co}_3\text{O}_4/\text{CeO}_2$  Nano-hybrids. *Adv. Mater.* **2019**, *31*, 1900062.

(53) Hou, Y.; Wang, J.; Liu, J.; Hou, C.; Xiu, Z.; Fan, Y.; Zhao, L.; Zhai, Y.; Li, H.; Zeng, J.; Gao, X.; Zhou, S.; Li, D.; Li, Y.; Dang, F.; Liang, K.; Chen, P.; Li, C.; Zhao, D.; Kong, B. Interfacial Super-Assembled Porous  $\text{CeO}_2/\text{C}$  Frameworks Featuring Efficient and Sensitive Decomposing  $\text{Li}_2\text{O}_2$  for Smart Li– $\text{O}_2$  Batteries. *Adv. Energy Mater.* **2019**, *9*, 1901751.

(54) Sun, H.; Tian, C.; Fan, G.; Qi, J.; Liu, Z.; Yan, Z.; Cheng, F.; Chen, J.; Li, C. P.; Du, M. Boosting Activity on  $\text{Co}_4\text{N}$  Porous Nanosheet by Coupling  $\text{CeO}_2$  for Efficient Electrochemical Overall Water Splitting at High Current Densities. *Adv. Funct. Mater.* **2020**, *30*, 1910596.

(55) Anandan, C.; Bera, P. XPS Studies on the Interaction of  $\text{CeO}_2$  with Silicon in Magnetron Sputtered  $\text{CeO}_2$  Thin Films on Si and  $\text{Si}_3\text{N}_4$  Substrates. *Appl. Surf. Sci.* **2013**, *283*, 297–303.

(56) Maslakov, K. I.; Teterin, Y. A.; Popel, A. J.; Teterin, A. Y.; Ivanov, K. E.; Kalmykov, S. N.; Petrov, V. G.; Petrov, P. K.; Farnan, I. XPS Study of Ion Irradiated and Unirradiated  $\text{CeO}_2$  Bulk and Thin Film Samples. *Appl. Surf. Sci.* **2018**, *448*, 154–162.

(57) Zheng, X.; Mofarah, S. S.; Cazorla, C.; Daiyan, R.; Esmailpour, A. A.; Scott, J.; Yao, Y.; Lim, S.; Wong, V.; Chen, E. Y.; Arandiyani, H.; Koshy, P.; Sorrell, C. C. Decoupling the Impacts of Engineering Defects and Band Gap Alignment Mechanism on the Catalytic Performance of Holey 2D  $\text{CeO}_{2-x}$ -Based Heterojunctions. *Adv. Funct. Mater.* **2021**, *31*, 2103171.

(58) Aškrabić, S.; Dohčević-Mitrović, Z.; Araújo, V. D.; Ionita, G.; Lima, M. M., Jr.; Cantarero, A. F.-C. Luminescence in Nanocrystalline  $\text{CeO}_2$ . *J. Phys. D: Appl. Phys.* **2013**, *46*, 495306.

(59) Liu, Y.; Jiang, S. P.; Shao, Z. Intercalation Pseudocapacitance in Electrochemical Energy Storage: Recent Advances in Fundamental Understanding and Materials Development. *Mater. Today Adv.* **2020**, *7*, 100072.

(60) Maheswari, N.; Muralidharan, G. Supercapacitor Behavior of Cerium Oxide Nanoparticles in Neutral Aqueous Electrolytes. *Energy Fuels* **2015**, *29*, 8246–8253.

(61) Willardson, R. K.; Beer, A. C. *Semiconductors and Semimetals*; Elsevier: London, U.K., 1977.

(62) Liu, T. C.; Pell, W. G.; Conway, B. E.; Roberson, S. L. Behavior of Molybdenum Nitrides as Materials for Electrochemical Capacitors: Comparison with Ruthenium Oxide. *J. Electrochem. Soc.* **1998**, *145*, 1882.

(63) Wang, J.; Polleux, J.; Lim, J.; Dunn, B. Pseudocapacitive Contributions to Electrochemical Energy Storage in  $\text{TiO}_2$  (Anatase) Nanoparticles. *J. Phys. Chem. C* **2007**, *111*, 14925–14931.

(64) Pallab, B.; Fornari, R.; Kamimura, H. *Comprehensive Semiconductor Science and Technology*; Elsevier Science: Oxford, U.K., 2011.

(65) Bahmanrokh, G.; Cazorla, C.; Mofarah, S. S.; Shahmiri, R.; Yao, Y.; Ismail, I.; Chen, W.-F.; Koshy, P.; Sorrell, C. C. Band Gap Engineering of Ce-Doped Anatase  $\text{TiO}_2$  through Solid Solubility Mechanisms and New Defect Equilibria Formalism. *Nanoscale* **2020**, *12*, 4916–4934.

(66) Arandiyani, H.; Mofarah, S. S.; Sorrell, C. C.; Doustkhah, E.; Sajjadi, B.; Hao, D.; Wang, Y.; Sun, H.; Ni, B.-J.; Rezaei, M.; Shao, Z.; Maschmeyer, T. Defect Engineering of Oxide Perovskites for Catalysis and Energy Storage: Synthesis of Chemistry and Materials Science. *Chem. Soc. Rev.* **2021**, *50*, 10116–10211.